

Transmission and Reflection of Bose-Einstein Condensates Incident on a Gaussian Potential Barrier

A.M. Martin¹, R.G. Scott^{2,3} and T.M. Fromhold³

¹ *School of Physics, University of Melbourne, Parkville, Victoria 3010, Australia*

² *Department of Physics, University of Otago, P.O. Box 56, Dunedin, New Zealand*

³ *School of Physics and Astronomy, University of Nottingham, Nottingham NG7 2RD, United Kingdom*

(Dated: August 29, 2018)

We investigate how Bose-Einstein condensates, whose initial state is either irrotational or contains a single vortex, scatter off a one-dimensional Gaussian potential barrier. We find that for low atom densities the vortex structure within the condensate is maintained during scattering, whereas at medium and high densities, multiple additional vortices can be created by the scattering process, resulting in complex dynamics and disruption of the atom cloud. This disruption originates from two different mechanisms associated respectively with the initial rotation of the atom cloud and the interference between the incident and reflected matter waves. We investigate how the reflection probability depends on the vorticity of the initial state and on the incident velocity of the Bose-Einstein condensate. To interpret our results, we derive a general analytical expression for the reflection coefficient of a rotating Bose-Einstein condensate that scatters off a spatially-varying one-dimensional potential.

PACS numbers: 03.75.Kk, 05.30.Jp, 67.40.Vs

I. INTRODUCTION

Recently, several experiments have investigated the scattering of Bose-Einstein condensates (BECs). These experiments have included Bragg reflection in an optical lattice [1], reflection from optical [2] and magnetic [3] mirrors, diffraction from a grating [4] and quantum reflection from a silicon surface [5]. In each case, interest has focused on the reflected component of the BEC. For example, investigations of quantum reflection from a silicon surface have revealed that inter-atomic interactions have a dramatic effect on the internal structure of the atom cloud [5, 6]. So far, reflection experiments have been restricted to condensates whose initial state contains no dynamical excitations. However, the methodology for creating and observing vortices in BECs is well established [7, 8, 9, 10] and, in the case of Bragg reflection, numerical simulations predict that vortices and solitons in the BEC's initial state strongly influence the subsequent dynamics [11]. Previous theoretical work has also shown that the presence of a vortex in the initial state can have a pronounced effect on the internal structure of a BEC that undergoes classical reflection from a hard wall atom mirror [12, 13]. To our knowledge, however, there has been no consideration of the effect of vortices on BECs approaching a potential barrier of *finite* width and height, where quantum-mechanical tunneling is possible as well as reflection. Quantum tunneling of BECs can be studied experimentally by using sheets of laser light to create the potential barrier [14] and plays a crucial role in the dynamics and macroscopic coherence of cold atoms in optical lattices [15].

In this paper, we investigate how BECs scatter off a Gaussian potential barrier, which allows both reflection and quantum-mechanical tunneling of the atoms. We use numerical simulations of the Gross-Pitaevskii equation to

make a detailed study of how the strength of the inter-atomic interactions, the energy of the incident BEC, and the vorticity of the initial state affect the scattering properties of the condensate. Our simulations reveal regimes in which dynamical excitations disrupt both the reflected and transmitted atom clouds. In one regime, which we call *rotational disruption*, the excitations originate from the effect of the initial vortex on the scattering dynamics. By contrast, the regime of *interferential disruption* [16] occurs both in the presence and absence of a vortex in the initial state with the excitations being created from interference between the incident and reflected matter waves. We find that rotational disruption arises when the time taken for the BEC to scatter is comparable with, or exceeds, the rotational period of the vortex. Interferential disruption occurs when the scattering time is greater than the correlation time of the BEC, which is a measure of how quickly the atom cloud responds to a perturbation. To interpret our results, we derive a general expression for the reflection probability of a BEC containing a vortex in terms of the reflection probability of an irrotational BEC. We find that the vortex changes the reflection probability by altering the distribution of incident velocities at the barrier, due to the increase in the physical size of the cloud and, more importantly, the circulation of the atoms.

To investigate the regimes of rotational and interferential disruption we consider three BECs whose initial state contains a single vortex: BEC *A* with low atom density, BEC *B* with medium density and BEC *C* with high density. We identify the effect of the initial vortex by comparing the dynamics of these atom clouds with irrotational counterparts labeled BECs A_i , B_i and C_i .

The layout of the paper is as follows: in section II we specify the parameters for each of the three BECs and describe the theoretical model and computational tech-

niques. In section III, we present our numerical results, which show how low, medium, and high density BECs scatter off the Gaussian potential barrier, both with and without a vortex in the initial state. In section IV, we derive a general expression for the reflection probability of an irrotational BEC. We then use this expression to derive an approximate analytical formula for the reflection probability of a condensate whose initial state *does* contain a vortex, impinging on the same scattering potential. We compare this formula with reflection probabilities obtained directly from the numerical simulations presented in section III and use it to provide physical insight into the effect of vortices on the scattering process. Finally, in section V, we summarize our results and propose experiments to test them.

II. SYSTEM PARAMETERS, THEORETICAL MODEL, AND COMPUTATIONAL TECHNIQUES

Each BEC contains N ^{23}Na atoms of mass m and is initially confined by a harmonic trapping potential, $V_T(x, y, z) = m[\omega_x^2(x + \Delta x)^2 + \omega_y^2 y^2 + \omega_z^2 z^2]/2$ centered at $(-\Delta x, 0, 0)$. We consider trap frequencies $\omega_x = \omega_y = 50 \times 2\pi \text{ rad s}^{-1} \ll \omega_z$ so that the spatial width of the BEC is much smaller along the z -direction than along the x - and y -directions. Consequently, the dynamics reduce to two-dimensional motion in the $x - y$ plane. At time $t = 0$, we create an additional Gaussian potential barrier [14]

$$V_L(x) = V_0 e^{-\frac{x^2}{\sigma^2}}, \quad (1)$$

of width $\sigma = 1 \mu\text{m}$ along the x -direction, by switching on a far blue-detuned laser beam that travels along the y -direction and creates a sheet of laser light. The intensity of the laser beam determines the barrier height, V_0 , which we take to be 6.2 peV , similar to recent experiments [14]. Simultaneously, we accelerate the BEC towards the Gaussian potential by abruptly displacing the harmonic trap through a distance Δx along the x -direction [4, 5, 6]. After the displacement, the center of the trap coincides with the Gaussian potential energy barrier and the total potential energy of the trap and laser beam, for motion in the $x - y$ plane, is given by

$$V(x, y) = m(\omega_x^2 x^2 + \omega_y^2 y^2)/2 + V_L(x). \quad (2)$$

The solid curve in Fig 1(a) shows the form of $V(x, y = 0)$. After the displacement of the harmonic trap, the condensate moves away from its initial state [shown schematically by the dashed curve in Fig. 1(a)], reaches the Gaussian potential with a mean incident velocity $\bar{v}_x \approx \omega_x \Delta x$, and is then scattered by the potential barrier.

The time-dependent Gross-Pitaevskii equation for the system is

$$i\hbar \frac{\partial \Psi(x, y, t)}{\partial t} = -\frac{\hbar^2}{2m} \left[\frac{\partial^2}{\partial x^2} + \frac{\partial^2}{\partial y^2} \right] \Psi(x, y, t)$$

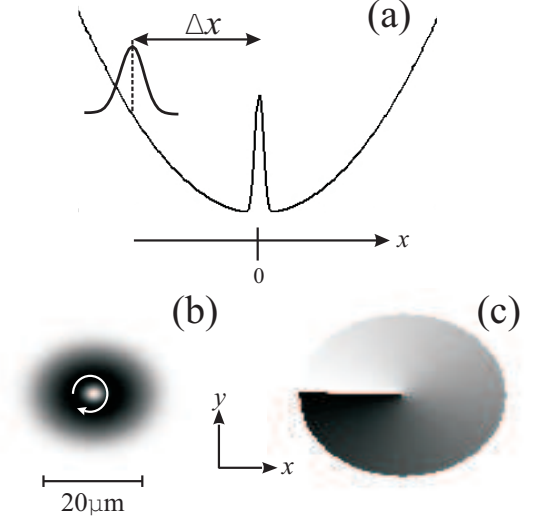


FIG. 1: (a) Solid curve: A schematic of the potential energy $V(x, y = 0)$ created by the harmonic trap and laser beam when $t \geq 0$; Dashed curve: a schematic of the initial probability density $|\Psi(x, y = 0, t = 0)|^2$ for BEC B . (b) The initial density $|\Psi(x, y, t = 0)|^2$ (black=high density, white=zero) of BEC B , where the white arrow shows the direction of the condensate's circulation and the horizontal bar denotes the scale. (c) The equivalent phase plot, $\phi(x, y, t = 0)$, (white= 0 , black= 2π).

$$+ [V(x, y) + U_0 |\Psi(x, y, t)|^2] \Psi(x, y, t) \quad (3)$$

where $\Psi(x, y, t)$ is the wavefunction for motion in the $x - y$ plane at time $t \geq 0$ and $U_0 = 4\pi\hbar^2 a/m$ where the s -wave scattering length $a = 2.9 \text{ nm}$.

We determine the initial BEC wave function by solving Eq. (3) for $t \leq 0$ using an imaginary time algorithm [17]. When the initial state contains a vortex, we impose the requirement that there is a 2π -phase change in the condensate wavefunction around the trap center at $(x, y) = (-\Delta x, 0)$, which corresponds to a quantized angular momentum of $-\hbar$ about the z -axis. The wavefunction is normalized according to

$$\int |\Psi(x, y, t)|^2 dx dy = \frac{N}{L_z}, \quad (4)$$

where L_z is the confinement length in the z -direction. For BECs A , B and C we choose N/L_z as $2.5 \times 10^8 \text{ m}^{-1}$, $5 \times 10^9 \text{ m}^{-1}$ and $2.5 \times 10^{11} \text{ m}^{-1}$ respectively, which gives corresponding peak atom densities $n_0 = 2.8 \times 10^{18} \text{ m}^{-3}$, $2.1 \times 10^{19} \text{ m}^{-3}$ and $1.6 \times 10^{20} \text{ m}^{-3}$. The density, $|\Psi(x, y, t = 0)|^2$, and phase, $\phi(x, y, t = 0)$, of the initial state for BEC B are shown in Figs. 1(b,c). Having obtained the initial state of the BEC, we determine its motion by solving the Gross-Pitaevskii equation (3) numerically using the Crank-Nicolson method [18].

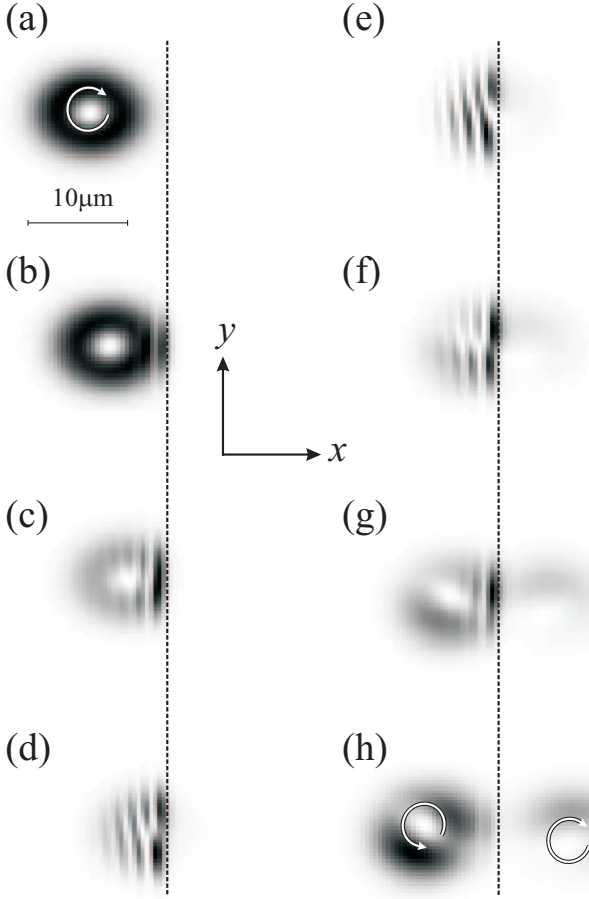


FIG. 2: Evolution of BEC A: plots of $|\Psi(x, y, t)|^2$ (black=high density, white=zero) for $\bar{v}_x = 6.3 \text{ mm s}^{-1}$ at $t = 3.6 \text{ ms}$ (a), 4.0 ms (b), 4.4 ms (c), 4.8 ms (d), 5.2 ms (e), 5.6 ms (f), 6.0 ms (g) and 6.4 ms (h). Coordinate axes are inset and the horizontal bar indicates the scale. The arrows in (a) and (h) show the direction of rotation.

III. NUMERICAL RESULTS FOR SCATTERING OFF A GAUSSIAN POTENTIAL BARRIER

In Fig. 2, we show the density profile of BEC A, with $\Delta x = 20 \mu\text{m}$ ($\bar{v}_x = 6.3 \text{ mm s}^{-1}$) at $t = 3.6 \text{ ms}$ (a), 4.0 ms (b), 4.4 ms (c), 4.8 ms (d), 5.2 ms (e), 5.6 ms (f), 6.0 ms (g) and 6.4 ms (h). Figs. 2(a-e) show that as the BEC approaches the Gaussian scattering potential at $x = 0$ (dashed lines in Fig. 2), a standing wave forms due to interference between the incoming and reflected matter-waves. In Figs. 2(d,e) the standing wave undergoes a π phase shift between the upper (large y) and lower (small y) edges of the BEC. This is due to the non-uniform initial phase of the BEC, shown in Fig. 1(c). After scattering, the BEC splits into reflected ($x < 0$) and transmitted ($x > 0$) components [Figs. 2(f-h)]. Each of the components contains a vortex [enclosed by the arrows in Fig. 2(h)]. For the transmitted cloud, the quantized circulation is in the same direction as in the incident cloud. By contrast, the reflected cloud rotates in the opposite direction [12, 13]. Physically, this is because atoms towards

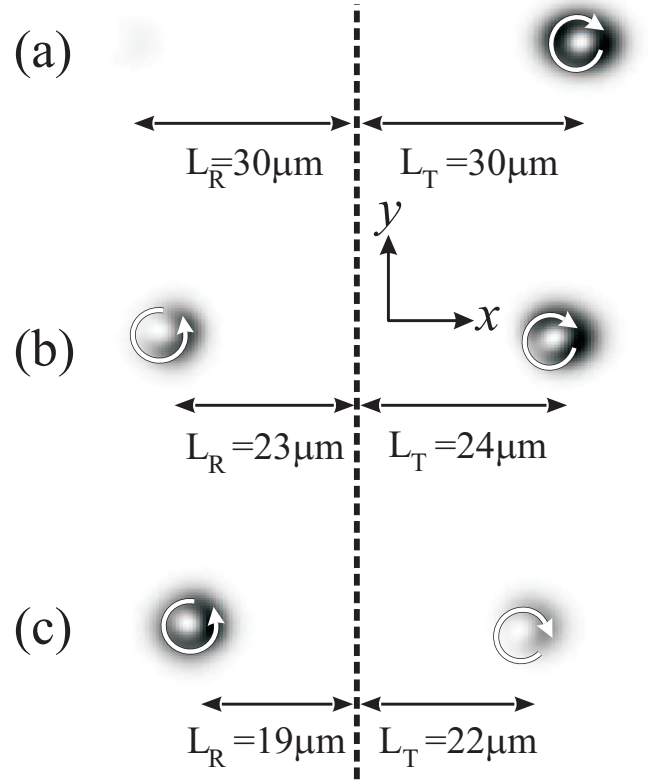


FIG. 3: BEC A: plots of $|\Psi(x, y, t = 10 \text{ ms})|^2$ for $\bar{v}_x = 9.4 \text{ mm s}^{-1}$ (a), 7.5 mm s^{-1} (b) and 6.3 mm s^{-1} (c). The circular arrows indicate the direction of rotation and the horizontal arrows show the values of L_R and L_T , defined in the text and footnote [19]. Co-ordinate axes are inset.

the top of the rotating incident cloud, in Fig. 2, approach the barrier with a higher velocity component along the x -direction (v_x) than those at the bottom. But because v_x is reversed after reflection, the direction of rotation is also reversed in the reflected cloud. This is in contrast to the transmitted atoms, which emerge through the barrier with little change in their velocity and so the direction of rotation is preserved. Since the trap remains switched on throughout the scattering process, we do not observe the splitting of the reflected component of the BEC that was reported in Ref. [13].

We now consider how changing \bar{v}_x affects the dynamics of the atom cloud. Figure 3 shows the density profile of BEC A at $t = \pi/\omega_x = 10 \text{ ms}$ after trap displacements of $30 \mu\text{m}$ (a), $24 \mu\text{m}$ (b) and $20 \mu\text{m}$ (c), corresponding to $\bar{v}_x = 9.4 \text{ mm s}^{-1}$, 7.5 mm s^{-1} and 6.3 mm s^{-1} respectively. Since this time is half the period of oscillation of the trap, both the transmitted and reflected portions of the condensate will *approximately* be at their turning points, and hence *nearly* stationary. In Fig. 3, the vertical dashed line marks the trap center at $x = 0$. When $\bar{v}_x = 9.4 \text{ mm s}^{-1}$, the average kinetic energy of the atoms incident upon the barrier is 10 peV , which exceeds the Gaussian barrier height. Hence, most of the condensate is transmitted [Fig. 3(a)]. As we decrease \bar{v}_x [Figs. 3(b,c)],

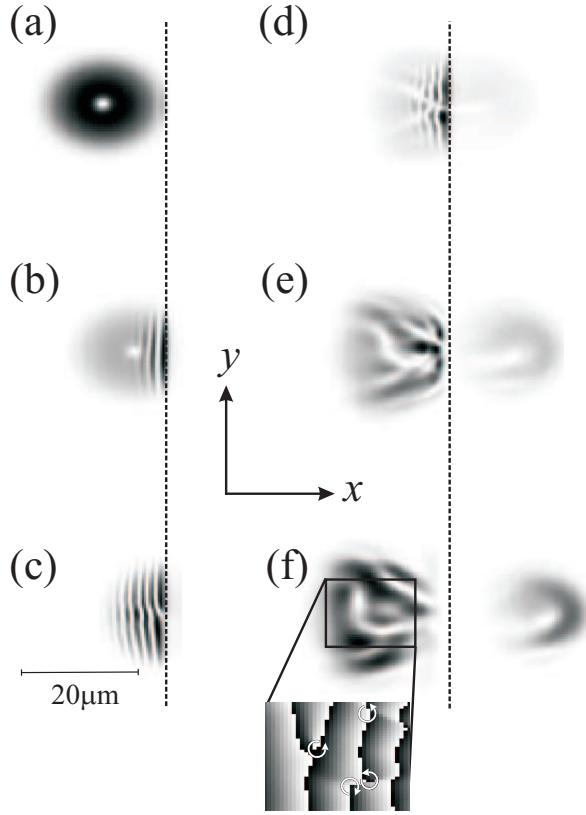


FIG. 4: Evolution of BEC B : plots of $|\Psi(x, y, t)|^2$ (black=high density, white=zero) for $\bar{v}_x = 6.3 \text{ mm s}^{-1}$ at $t = 3 \text{ ms}$ (a), 4 ms (b), 5 ms (c), 6 ms (d), 7 ms (e), 8 ms (f). The dashed line at $x = 0$ marks the point where the laser potential is maximal. Co-ordinate axes are inset and the horizontal bar indicates scale. Lower plot: phase $\phi(x, y, t = 8 \text{ ms})$ [white= 0, black= 2π] within the region enclosed by the box in (f). Arrows indicate the direction of circulation.

the average energy of the incident atoms decreases and more of the condensate is reflected. For $\bar{v}_x = 6.3 \text{ mm s}^{-1}$ [Fig. 3(c)], most of the atoms are reflected by the barrier because the average kinetic energy of the incident atoms is 4.6 peV , which is less than the barrier height. Since the BEC has a finite spatial width along the x -direction of $l_x = 13 \mu\text{m}$, atoms that are towards the left-hand side of the BEC's initial state travel further before reaching the barrier and therefore have a higher incident velocity. Such atoms have a higher transmission probability and therefore form a large fraction of the transmitted atom cloud. We therefore expect that the distance (L_T) that the higher velocity transmitted cloud travels past the scattering potential before coming to rest in the harmonic trap will be greater than the distance (L_R) that the slower reflected cloud retreats from the scatterer before reaching the turning point of the harmonic trap [19]. Our numerical simulations confirm this: for example, in Fig. 3, $L_T \geq L_R$ for all the values of \bar{v}_x .

We now consider how the higher density BEC B reflects off the potential barrier. Figure 4 shows the density profile of BEC B at $t = 3 \text{ ms}$ (a), 4 ms (b), 5 ms (c),

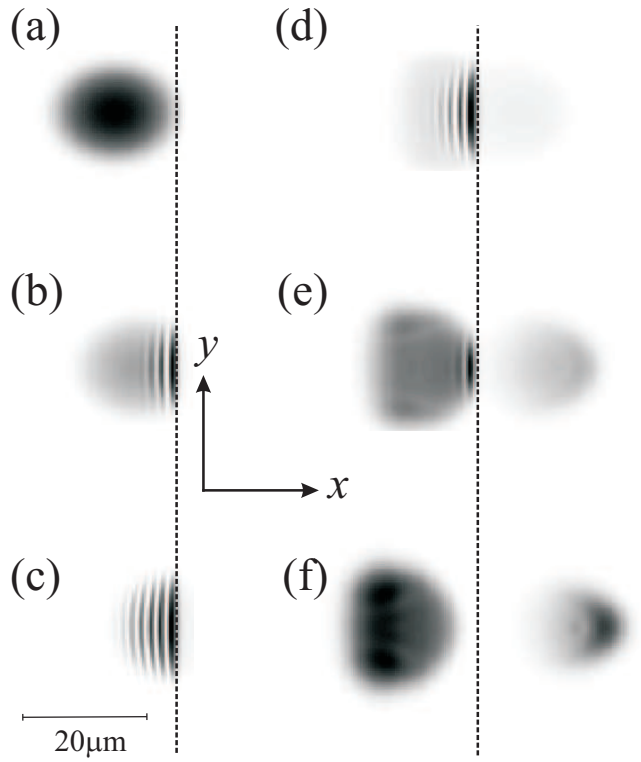


FIG. 5: Evolution of BEC B_i : plots of $|\Psi(x, y, t)|^2$ (black=high density, white=zero) for $\bar{v}_x = 6.3 \text{ mm s}^{-1}$ at $t = 3 \text{ ms}$ (a), 4 ms (b), 5 ms (c), 6 ms (d), 7 ms (e), 8 ms (f). The dashed line at $x = 0$ marks the point where the laser potential is maximal. Co-ordinate axes are inset and the horizontal bar indicates scale.

6 ms (d), 7 ms (e) and 8 ms (f), after a trap displacement of $20 \mu\text{m}$ ($\bar{v}_x = 6.3 \text{ mm s}^{-1}$). As the BEC impinges upon the Gaussian potential barrier, a standing wave forms between the incoming and reflected matter waves. Figure 4(b) shows the first stage of the standing wave formation in which maxima (black) and nodal lines (white) appear at the leading edge of the atom cloud. In contrast to BEC A , the reflected component of the BEC is significantly disrupted, as shown in Figs. 4(e,f). This disruption is accompanied by the formation of *new* vortices within the boxed region in Fig. 4(f). The phase variation, $\phi(x, y, t = 8 \text{ ms})$, within this region is shown in the lower part of Fig. 4(f). Around each vortex, ϕ increases from 0 to 2π in the direction of circulation shown by the arrows in Fig. 4(f).

To explain the disruption shown in Fig. 4, we first consider the dynamics of BEC B_i . Figure 5 shows density profiles for this initially irrotational condensate at $t = 3 \text{ ms}$ (a), 4 ms (b), 5 ms (c), 6 ms (d), 7 ms (e) and 8 ms (f) after a trap displacement $20 \mu\text{m}$ ($\bar{v}_x = 6.3 \text{ mm s}^{-1}$). No dynamical excitations are produced in the transmitted or reflected clouds. We therefore conclude that the disruption observed for BEC B (Fig. 4) is related to the rotation of the cloud.

To gain further insights into this disruption, we now examine how changing \bar{v}_x affects the transmission and re-

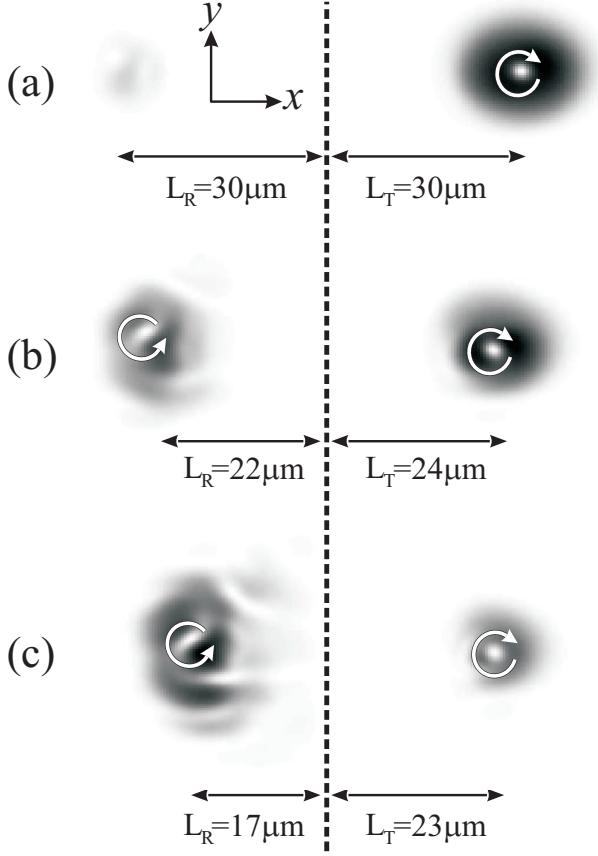


FIG. 6: BEC *B*: plots of $|\Psi(x, y, t = 10 \text{ ms})|^2$ for $\bar{v}_x = 9.4 \text{ mm s}^{-1}$ (a), $\bar{v}_x = 7.5 \text{ mm s}^{-1}$ (b) and $\bar{v}_x = 6.3 \text{ mm s}^{-1}$ (c). The dashed line at $x = 0$ marks the point where the laser potential is maximal. The circular arrows indicate the direction of rotation and the horizontal arrows show the values of L_R and L_T , defined in the text and footnote [19]. Co-ordinate axes are inset.

flection of BEC *B*. Figure 6 shows the condensate density at $t = 10 \text{ ms}$ after trap displacements of $\Delta x = 30 \mu\text{m}$ (a), $24 \mu\text{m}$ (b), and $20 \mu\text{m}$ (c), corresponding to mean incident velocities of $\bar{v}_x = 9.4 \text{ mm s}^{-1}$, 7.5 mm s^{-1} and 6.3 mm s^{-1} respectively. For $\bar{v}_x = 9.4 \text{ mm s}^{-1}$, the behavior of BEC *B* [Fig. 6(a)] is qualitatively the same as BEC *A* [Fig. 3(a)]: the transmitted cloud retains the vortex structure of the incident cloud and only a small fraction of atoms are reflected. As \bar{v}_x decreases [Figs. 6(b,c)], the reflection probability rises, but the structure of the reflected cloud becomes increasingly disrupted. This disruption contrasts with BEC *A*, where for all \bar{v}_x values the reflected cloud retains a well defined vortex structure (Fig. 3). For BEC *B*, we find that $L_T \geq L_R$ (see values in Fig. 6) just as for BEC *A*. However, for $\bar{v}_x = 7.5 \text{ mm s}^{-1}$ and $\bar{v}_x = 6.3 \text{ mm s}^{-1}$, L_R is lower for BEC *B* [Fig. 6(b,c)] than for BEC *A* [Fig. 3(b,c)] due to the fragmentation of the atom cloud that occurs for BEC *B* only. This fragmentation transfers kinetic energy from the center-of-mass motion of the reflected cloud into internal vorticity, thus damping the oscillation.

The effect of the vortex on the scattering process depends on the scattering time of the vortex core (t_{sv}) relative to its rotation time (t_r). Since the diameter of the vortex core is approximately the healing length $\xi = 1/\sqrt{8\pi n_0 a}$, it follows that $t_{sv} \approx 2\xi/\bar{v}_x$ and $t_r = \pi\xi^2 m/\hbar$. If the ratio

$$\frac{t_r}{t_{sv}} = \frac{m}{2\hbar} \pi \xi \Delta x \omega_x \propto \frac{\Delta x}{\sqrt{n_0}} \quad (5)$$

is $\gg 1$, so that there is insufficient time for the vortex to rotate during the scattering process, the vortex will have little effect on the dynamics of the transmitted and reflected atom clouds. Physically, this is because all parts of the BEC are incident on the Gaussian potential with a variation in the incident velocity, due to the rotation, that is small compared to \bar{v}_x . Conversely, if $t_r/t_{sv} \lesssim 1$ we expect that the rotation of the BEC will disrupt the reflected component of the BEC. We refer to such a regime as rotational disruption. For the lower-density BEC *A*, $t_r/t_{sv} \gg 1$ for all three of the \bar{v}_x values considered in Fig. 3, and so the reflected atom cloud is not significantly fragmented. By contrast, for the higher density BEC *B* $t_r/t_{sv} < 1$, and hence rotational disruption occurs in the reflected atom cloud. Note that reducing \bar{v}_x from 9.4 mm s^{-1} [Fig. 6(a)] to 6.3 mm s^{-1} [Fig. 6(c)] causes t_r/t_{sv} to decrease, and thus increases the fragmentation of the reflected cloud.

Disruption of the reflected cloud is even more pronounced for the higher density BEC *C*. Figure 7 shows the density of this BEC at $t = 1 \text{ ms}$ (a), 2 ms (b), 3 ms (c), 4 ms (d), 5 ms (e), 6 ms (f), 7 ms (g) and 8 ms (h) after a trap displacement of $30 \mu\text{m}$ ($\bar{v}_x = 9.4 \text{ mm s}^{-1}$) [20]. As the condensate impinges upon the scattering potential, a standing wave forms between the incident and reflected matter waves, Figs. 7(b-d). This standing wave seeds solitons [6, 21, 22], which decay via the snake instability [24] into vortex-antivortex pairs [Figs. 7(e,f)], thus strongly disrupting the internal structure of the cloud [Figs. 7(g,h)]. Consequently, when incident atoms subsequently pass through the barrier they produce some irregularity in the transmitted atom cloud. Note, that this irregularity is less pronounced towards the right hand edge of the transmitted cloud, which contains the atoms that passed through the barrier *before* solitons and vortices formed at negative x ($x = 0$ is marked by the dotted line in Fig. 7). We emphasize that although BEC *C* is in a regime where rotational disruption occurs, the initial vortex does *not* (in contrast to BEC *B*) cause the severe fragmentation shown in Fig. 7. To demonstrate this, Fig. 8 shows BEC *C_i* (identical to BEC *C*, except irrotational) scattering off a Gaussian potential at $t = 1 \text{ ms}$ (a), 2 ms (b), 3 ms (c), 4 ms (d), 5 ms (e), 6 ms (f), 7 ms (g) and 8 ms (h) after a trap displacement of $30 \mu\text{m}$ ($\bar{v}_x = 9.4 \text{ mm s}^{-1}$). Comparison of Figs. 7 and 8 reveals that the dynamics are qualitatively the same irrespective of whether or not the BEC contains an initial vortex.

To understand these results, we recall previous work [11, 21, 22, 23] on the Bragg reflection of a BEC in an op-

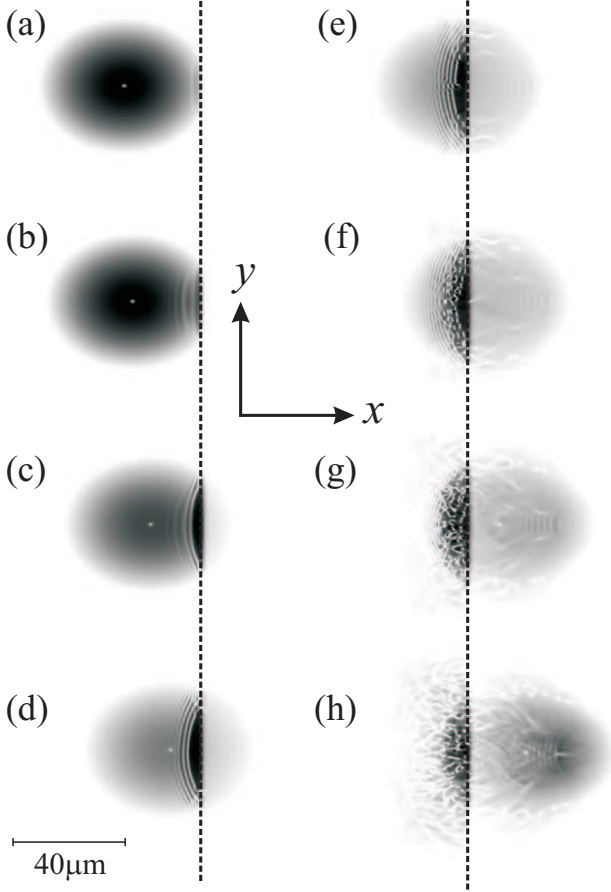


FIG. 7: Evolution of BEC C : plots of $|\Psi(x, y, t)|^2$ (black=high density, white=zero) for $\bar{v}_x = 9.4 \text{ mm s}^{-1}$ at $t = 1 \text{ ms}$ (a), 2 ms (b), 3 ms (c), 4 ms (d), 5 ms (e), 6 ms (f), 7 ms (g) and 8 ms (h). Co-ordinate axes are inset and the horizontal bar indicates the scale.

tical lattice. In Refs. [21, 22] it was shown that at Bragg reflection, fragmentation can arise from the density and phase imprinting that accompanies standing wave formation. When the correlation time,

$$t_c = \frac{m}{2\sqrt{2}\hbar n_0 a}, \quad (6)$$

is much less than the Bloch period (t_B), this imprinting leads to the formation of solitons and vortices, which disrupt the atom cloud. For BECs C and C_i , a similar disruption occurs when $t_c \ll t_s$, where $t_s = l_x/\bar{v}_x$ is the approximate duration of the reflection process. This effect is described as *interferential disruption* [16], since it originates from the interference pattern, in this case produced by the superposition of the incident and reflected matter waves. For BEC C this interferential disruption dominates the dynamics and completely masks any effects due to the rotational disruption.

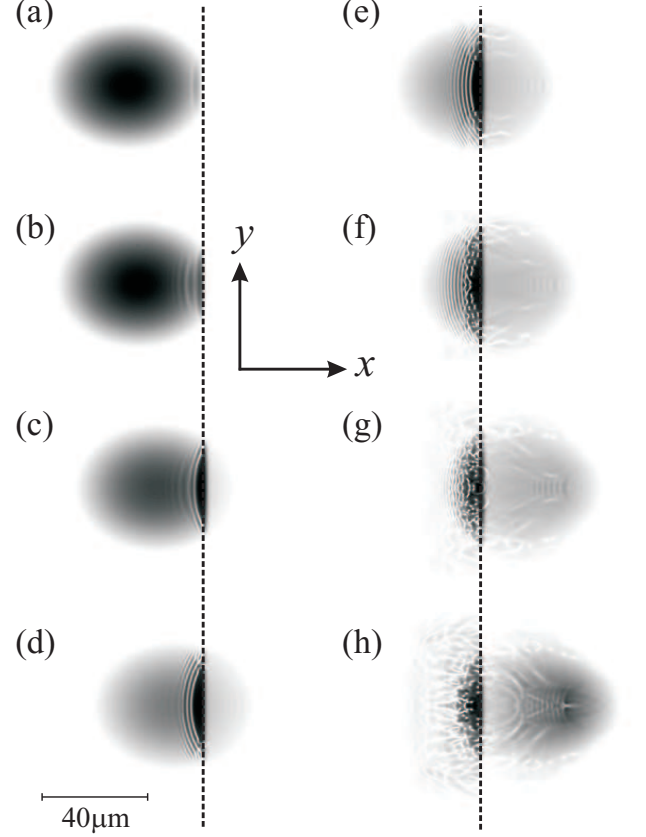


FIG. 8: Evolution of BEC C_i : plots of $|\Psi(x, y, t)|^2$ (black=high density, white=zero) for $\bar{v}_x = 9.4 \text{ mm s}^{-1}$ at $t = 1 \text{ ms}$ (a), 2 ms (b), 3 ms (c), 4 ms (d), 5 ms (e), 6 ms (f), 7 ms (g) and 8 ms (h). Co-ordinate axes are inset and the horizontal bar indicates the scale.

IV. REFLECTION PROBABILITY OF THE BEC

In this section, we investigate how the reflection probability of the BEC varies with \bar{v}_x and depends on the presence or absence of an initial vortex. Defining the reflection probability of the condensate as

$$R(\bar{v}_x = \Delta x \omega_x) = \frac{\int_y \int_{x<0} |\Psi(x, y, t = \pi/\omega_x)|^2 dx dy}{\int_y \int_x |\Psi(x, y, t)|^2 dx dy}, \quad (7)$$

we use our numerical solution of the Gross-Pitaevskii equation to quantify the reflection probabilities of BEC A [$R(\bar{v}_x)$, dotted curve in Fig. 9(a)] and its irrotational equivalent [$R_i(\bar{v}_x)$, dashed curve in Fig. 9(a)]. Figure 9(a) shows that as \bar{v}_x decreases, both $R(\bar{v}_x)$ and $R_i(\bar{v}_x)$ increase. For $\bar{v}_x \lesssim 7.3 \text{ mm s}^{-1}$, $R(\bar{v}_x) < R_i(\bar{v}_x)$ and conversely for $\bar{v}_x \gtrsim 7.3 \text{ mm s}^{-1}$, $R(\bar{v}_x) > R_i(\bar{v}_x)$. This crossover is revealed more clearly by the dashed curve in Fig. 9(b), which shows $r(\bar{v}_x) = R(\bar{v}_x) - R_i(\bar{v}_x)$. For $\bar{v}_x \lesssim 7.3 \text{ mm s}^{-1}$, $r(\bar{v}_x) < 0$, but at higher \bar{v}_x , $r(\bar{v}_x) > 0$.

In Fig. 9(a) we compare $R(\bar{v}_x)$ and $R_i(\bar{v}_x)$ to the equivalent plane wave reflection probability $R_P(\bar{v}_x)$ (solid curve). The difference between $R_P(\bar{v}_x)$ and $R_i(\bar{v}_x)$

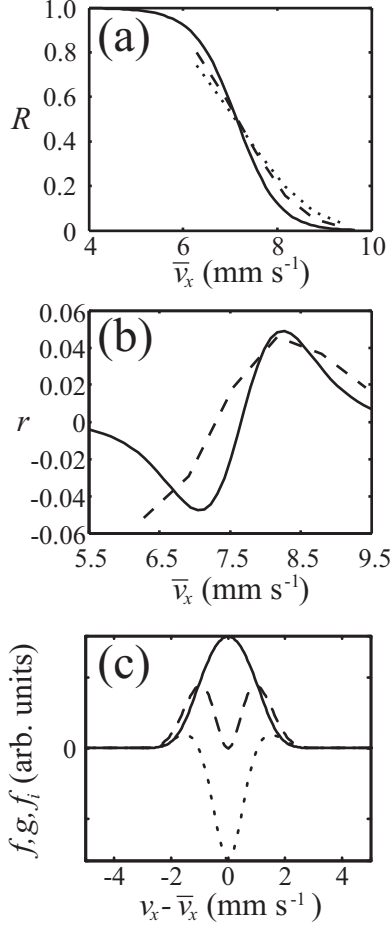


FIG. 9: (a) Dotted curve: reflection probability, $R(\bar{v}_x)$, for BEC A. Dashed curve: reflection probability, $R_i(\bar{v}_x)$, for BEC A_i . Solid curve: reflection probability, $R_P(\bar{v}_x)$, for a plane wave. (b) Dashed curve: $r(\bar{v}_x)$ obtained from numerical simulations. Solid curve: the expression for $r(\bar{v}_x)$ obtained from Eq. (18) with $I = 0.007 \text{ mm}^2 \text{ s}^{-2}$ and $J = 0.19 \text{ mm}^2 \text{ s}^{-2}$. (c) Solid curve: the local velocity distribution function, $f_i(v_x - \bar{v}_x, y = 0)$ for BEC A_i . Dashed curve: the local velocity distribution function, $f(v_x - \bar{v}_x, y = 0)$ for BEC A. Dotted curve: $g(v_x - \bar{v}_x, y = 0)$.

is due to the finite width of the BEC along the x -direction, which means that the atoms start from various positions in the harmonic trap and thus reach the barrier with a range of incident velocities rather than the single velocity of an incident plane wave. We can model the spread of velocities by defining the probability $F_i(v_x - \bar{v}_x)dv_x = \int_y f_i(v_x - \bar{v}_x, y)dydv_x$ that an atom arrives at the barrier with an incident velocity between v_x and $v_x + dv_x$. Here $f_i(v_x - \bar{v}_x, y)dv_x = |\Psi((v_x - \bar{v}_x)/\omega_x, y, t = 0)|^2 dv_x / \int_{v_x} |\Psi((v_x - \bar{v}_x)/\omega_x, y, t = 0)|^2 dv_x$ is the *local* probability that an atom starting from position y arrives at the barrier with a normal velocity component between v_x and $v_x + dv_x$. For each y , this local probability is determined from the initial shape of the BEC wavefunction, which defines the initial spatial distribution of the atoms and hence the resulting velocity

distribution as the atoms arrive at the barrier. For each y , $f_i(v_x - \bar{v}_x, y)$ is symmetrical about $v_x - \bar{v}_x = 0$ owing to the symmetry of the initial wavefunction. This can be seen from the solid curve in Fig. 9(c), which shows $f_i(v_x - \bar{v}_x, y = 0)$ for BEC A_i . The reflection probability of the BEC can be expressed in terms of its velocity distribution and the reflection probability of a plane wave by

$$R_i(\bar{v}_x) = \int_0^\infty F_i(v_x - \bar{v}_x) R_P(v_x) dv_x. \quad (8)$$

Since $F_i(v_x - \bar{v}_x)$ is sharply peaked at $v_x = \bar{v}_x$ we can use the Taylor expansion

$$R_P(v_x) \approx R_P(\bar{v}_x) + \left. \frac{\partial R_P(v_x)}{\partial v_x} \right|_{\bar{v}_x} (v_x - \bar{v}_x) + \left. \frac{\partial^2 R_P(v_x)}{2\partial v_x^2} \right|_{\bar{v}_x} (v_x - \bar{v}_x)^2 \quad (9)$$

to write Eq. (8) in the form

$$R_i(\bar{v}_x) \approx R_P(\bar{v}_x) \int_0^\infty F_i(v_x - \bar{v}_x) dv_x + \left. \frac{\partial R_P(v_x)}{\partial v_x} \right|_{\bar{v}_x} \int_0^\infty F_i(v_x - \bar{v}_x) (v_x - \bar{v}_x) dv_x + \left. \frac{\partial^2 R_P(v_x)}{2\partial v_x^2} \right|_{\bar{v}_x} \int_0^\infty F_i(v_x - \bar{v}_x) (v_x - \bar{v}_x)^2 dv_x. \quad (10)$$

Since $F_i(v_x - \bar{v}_x)$ is symmetrical about 0 and its width is less than \bar{v}_x for all the \bar{v}_x values considered in Figs. 9(a,b), Eq. (10) reduces to

$$R_i(\bar{v}_x) \approx R_P(\bar{v}_x) + \frac{I}{2} \left. \frac{\partial^2 R_P(v_x)}{\partial v_x^2} \right|_{\bar{v}_x}, \quad (11)$$

where [25]

$$I = \int_0^\infty F_i(v_x - \bar{v}_x) (v_x - \bar{v}_x)^2 dv_x > 0. \quad (12)$$

It follows from Eqs. (11) and (12) that $R_i(\bar{v}_x) > R_P(\bar{v}_x)$ if

$$\left. \frac{\partial^2 R_P(v_x)}{\partial v_x^2} \right|_{\bar{v}_x} > 0 \quad (13)$$

and $R_i(\bar{v}_x) < R_P(\bar{v}_x)$ if

$$\left. \frac{\partial^2 R_P(v_x)}{\partial v_x^2} \right|_{\bar{v}_x} < 0. \quad (14)$$

Evaluating the integral in Eq. (12) numerically, we find that for BEC A_i , $I = 0.007 \text{ mm}^2 \text{ s}^{-2}$.

From the shape of the solid curve in Fig. 9(a), we see that for $\bar{v}_x \lesssim 7.3 \text{ mm s}^{-1}$, $\left. \frac{\partial^2 R_P(v_x)}{\partial v_x^2} \right|_{\bar{v}_x} < 0$, whilst for

$\bar{v}_x \gtrsim 7.3 \text{ mm s}^{-1}$, $\left. \frac{\partial^2 R_P(v_x)}{\partial v_x^2} \right|_{\bar{v}_x} > 0$. Hence, from Eq. (11), we expect $R_i(\bar{v}_x) > R_P(\bar{v}_x)$, for $\bar{v}_x \gtrsim 7.3 \text{ mm s}^{-1}$, and $R_i(\bar{v}_x) < R_P(\bar{v}_x)$, for $\bar{v}_x \lesssim 7.3 \text{ mm s}^{-1}$, which is confirmed by comparing the dashed $[R_i(\bar{v}_x)]$ and solid $[R_P(\bar{v}_x)]$ curves in Fig. 9(a).

We now consider a BEC that initially contains a single vortex. In this case, Eq. (8) can be generalized to

$$R(\bar{v}_x) = \int_0^\infty F(v_x - \bar{v}_x) R_P(v_x) dv_x \quad (15)$$

where the velocity distribution for the incident atoms in the rotating BEC, $F(v_x - \bar{v}_x)$, equals the velocity distribution function for an irrotational BEC plus a correction $G(v_x - \bar{v}_x)$ that is

$$F(v_x - \bar{v}_x) = F_i(v_x - \bar{v}_x) + G(v_x - \bar{v}_x), \quad (16)$$

where $F(v_x - \bar{v}_x) = \int_y f(v_x - \bar{v}_x, y) dy$ and $G(v_x - \bar{v}_x) = \int_y g(v_x - \bar{v}_x, y) dy$ are defined in terms of the local velocity distribution functions $f(v_x - \bar{v}_x, y)$ and $g(v_x - \bar{v}_x, y) = f(v_x - \bar{v}_x, y) - f_i(v_x - \bar{v}_x, y)$, which are shown in Fig. 9(c), for $y = 0$, by the dashed and dotted curves respectively. Since $g(v_x - \bar{v}_x, y)$ and $G(v_x - \bar{v}_x)$ are both symmetrical about $v_x - \bar{v}_x = 0$, it follows from an analysis similar to that presented in Eqs. (8-10) that

$$R(\bar{v}_x) \approx R_i(\bar{v}_x) + \left. \frac{\partial^2 R_P(v_x)}{2 \partial v_x^2} \right|_{\bar{v}_x} \int_0^\infty G(v_x - \bar{v}_x) (v_x - \bar{v}_x)^2 dv_x, \quad (17)$$

which can be rewritten as

$$R(\bar{v}_x) \approx R_i(\bar{v}_x) + \frac{J}{2} \left. \frac{\partial^2 R_P(v_x)}{\partial v_x^2} \right|_{\bar{v}_x} \approx R_P(\bar{v}_x) + \frac{(I + J)}{2} \left. \frac{\partial^2 R_P(v_x)}{\partial v_x^2} \right|_{\bar{v}_x} \quad (18)$$

where

$$J = \int_0^\infty G(v_x - \bar{v}_x) (v_x - \bar{v}_x)^2 dv_x. \quad (19)$$

Unlike I , the sign of J can be either negative or positive, depending on the form of $G(v_x - \bar{v}_x)$. To highlight this, we initially consider a simple analysis based on the form of the local distribution function $g(v_x - \bar{v}_x, y = 0)$ [Fig. 9(c)]. For $v_x \approx \bar{v}_x$ (i.e. in the region of the vortex core) $f(v_x - \bar{v}_x, y = 0)$ [dashed curve in Fig. 9(c)] is close to zero, because the atom density falls to zero at the vortex core, whereas $f_i(v_x - \bar{v}_x, y = 0)$ [solid curve in Fig. (c)] is maximal. Consequently, $g(v_x - \bar{v}_x, y = 0)$ [dotted curve in Fig. 9(c)] is negative for $v_x \approx \bar{v}_x$. Since the atoms have moved away from the vortex core, towards the edges of the BEC, we expect that away from the vortex core (where $|v_x - \bar{v}_x| \gg 0$) $f(v_x - \bar{v}_x, y = 0) > f_i(v_x - \bar{v}_x, y = 0)$ and hence $g(v_x - \bar{v}_x, y = 0) > 0$, as

can be seen in Fig. 9(c) (dotted curve). Consequently, the contribution to J is likely to be positive because the integrand in Eq. (19) is largest when $(v_x - \bar{v}_x)^2$ is large.

However, if $y \neq 0$, v_x is also perturbed by the circulation of the BEC around the vortex core. For $y > 0$, v_x is increased and for $y < 0$, v_x is decreased. This effect further increases the spread of incident velocities at the barrier and, due to the $(v_x - \bar{v}_x)^2$ term in Eq. (19), makes J more positive. From our full numerical analysis we find that the dominant cause of the shift in the reflection probabilities is the circulation of atoms around the vortex. Evaluating Eq. (19) numerically, we find for BEC A that $J = 0.19 \text{ mm}^2 \text{ s}^{-2} \gg I$.

Since J and I are both positive for the BEC considered here, from Eqs. (11) and (18), we expect that $R(\bar{v}_x) - R_P(\bar{v}_x)$ will have the same sign as, but a larger magnitude than, $R_i(\bar{v}_x) - R_P(\bar{v}_x)$. This is confirmed by the curves shown in Fig. 9(a) and highlights the fact that the presence of the vortex increases the distribution of incident velocities upon the scattering potential.

In Fig. 9(b), we compare the expression for $r(\bar{v}_x) \approx \left. \frac{J}{2} \frac{\partial^2 R_P(v_x)}{\partial v_x^2} \right|_{\bar{v}_x}$, obtained from Eq. (18) (solid curve), with the numerical values of $r(\bar{v}_x)$ (dashed curve) obtained from our solutions of the Gross-Pitaevskii equation. The expression for $r(\bar{v}_x)$ (solid curve) and the numerical simulations (dashed curve) are in good agreement because the spread of incident velocities is narrow and hence the Taylor expansions used in the derivation of Eqs. (11) and (18) are reasonably accurate. For BEC B we find that the discrepancy between the numerical $r(\bar{v}_x)$ values and those obtained from Eq. (18) becomes larger. This discrepancy is not only due to an increase in the spread of incident velocities, which introduces higher order terms into the Taylor expansion, but also arises from the disruption of the BEC upon scattering, an effect which is not described in our approximate analysis. Equations. (11) and (18) are therefore only valid when no interferential or rotational disruption is present in the BEC.

V. CONCLUSIONS

We have investigated how BECs with different atom densities scatter off a Gaussian potential when the initial state is either irrotational or contains a single vortex. We find three distinct regimes for the formation of dynamical excitations and hence rotational or interferential disruption: (i) at low densities there is no fragmentation of the reflected or transmitted components of the BEC, irrespective of whether or not there is a vortex in the initial state; (ii) at medium densities for which $t_r/t_{sr} \lesssim 1$, rotational disruption occurs in the reflected component of a BEC with an initial vortex, but no disruption is observed when the BEC is initially irrotational; (iii) at high densities, there is strong interferential disruption in the reflected atom cloud if $t_c \lesssim t_s$, both in the presence and absence of an initial vortex.

By considering the velocity distribution of the incident atoms, we have derived expressions for the reflection probabilities of rotating and irrotational BECs in terms of the reflection probability of a single plane wave incident on the scattering potential. This analytic approach agrees well with our numerical calculations of reflection probabilities for BECs scattering from a Gaussian barrier. It shows that the velocity spread of an irrotational BEC causes a positive or negative deviation from $R_P(\bar{v}_x)$, depending on the curvature of $R_P(\bar{v}_x)$. When a vortex is introduced, the circulation further increases the spread

of incident velocities, leading to an even larger deviation from $R_P(\bar{v}_x)$.

Finally, we note that with current techniques it should be possible to perform experimental tests of our theoretical predictions, relating to the existence of three distinct dynamical regimes and to the effect of a vortex on the reflection probability of a BEC impinging on a potential barrier.

This work was supported by the ARC, the EPSRC, the Royal Society (London) and the University of Melbourne.

-
- [1] O. Morsch, J.H. Müller, M. Cristiani and E. Arimondo, Phys. Rev. Lett. **87**, 140402 (2001).
- [2] A. S. Arnold, C. MacCormick, and M. G. Boshier, Phys. Rev. A **65**, 031601 (2002).
- [3] K. Bongs, S. Burger, G. Birkel, K. Sengstock, W. Ertmer, K. Rzazewski, A. Sanpera, and M. Lewenstein, Phys. Rev. Lett. **83**, 3577 (1999).
- [4] A. Günther, S. Kraft, M. Kemmler, D. Koelle, R. Kleiner, C. Zimmermann and J. Fortágh, Phys. Rev. Lett. **95**, 170405 (2005).
- [5] T.A. Pasquini, Y. Shin, C. Sanner, M. Saba, A. Schrotzek, D.E. Pritchard, and W. Ketterle, Phys. Rev. Lett. **93**, 223201 (2004); T.A. Pasquini, M. Saba, G.-B. Jo, Y. Shin, W. Ketterle, D.E. Pritchard, T.A. Savas and N. Mulders, Phys. Rev. Lett. **97**, 093201 (2006).
- [6] R.G. Scott, A.M. Martin, T.M. Fromhold and F.W. Sheard, Phys. Rev. Lett. **95**, 073201 (2005).
- [7] M. R. Matthews, B. P. Anderson, P. C. Haljan, D. S. Hall, C. E. Wieman, and E. A. Cornell, Phys. Rev. Lett. **83**, 2498 (1999).
- [8] K. W. Madison, F. Chevy, W. Wohlleben, and J. Dalibard, Phys. Rev. Lett. **84**, 806 (2000).
- [9] F. Chevy, K. W. Madison, and J. Dalibard, Phys. Rev. Lett. **85**, 2223 (2000).
- [10] C. Raman, J. R. Abo-Shaer, J. M. Vogels, K. Xu, and W. Ketterle, Phys. Rev. Lett. **87**, 210402 (2001).
- [11] R.G. Scott, A.M. Martin and T.M. Fromhold, Phys. Rev. A **69**, 063607 (2004).
- [12] J.J. Garcia-Ripoll, G. Molina-Terriza, V. M. Perez-Garcia and L. Torner, Phys. Rev. Lett. **87**, 140403 (2001).
- [13] I. Josopait, L. Dobrek, L. Santos, A. Sanpera and M. Lewenstein, Eur. Phys. J. D. **22**, 385 (2003).
- [14] Y. Shin, M. Saba, T.A. Pasquini, W. Ketterle, D.E. Pritchard and A.E. Leanhardt, Phys. Rev. Lett. **92**, 050405 (2004).
- [15] M. Greiner, O. Mandel, T.W. Hänsch and I. Bloch, Nature **419**, 51 (2002).
- [16] R.G. Scott, D.A.W. Hutchinson and C.W. Gardiner, cond-mat/0608135 (unpublished).
- [17] M.L. Chiofalo, S. Succi and M.P. Tosi, Phys. Rev. E, **62**, 7438 (2000).
- [18] W.H. Press, S.A. Teukolsky, W.T. Vetterling and B.P. Flannery, *Numerical Recipes, the Art of Scientific Computing* (Cambridge University Press, Cambridge, 1994).
- [19] We calculate the expectation values of the positions of the transmitted and reflected atom clouds when they come to rest at $t = \pi/\omega_x$ as
- $$L_T = \frac{\int_y \int_{x>0} |\Psi(x, y; t = \pi/\omega_x)|^2 x dx dy}{\int_y \int_x |\Psi(x, y; t)|^2 dx dy}$$
- and
- $$L_R = \frac{\int_y \int_{x<0} |\Psi(x, y; t = \pi/\omega_x)|^2 x dx dy}{\int_y \int_x |\Psi(x, y; t)|^2 dx dy}.$$
- [20] Since the interactions in BEC *C* play a dominant role, the diameter of the condensate is $50\mu\text{m}$ and hence it is only possible to consider $\Delta x > 25\mu\text{m}$. For this reason we only consider $\Delta x = 30\mu\text{m}$ for system *C*.
- [21] R.G. Scott, A.M. Martin, T.M. Fromhold, S. Bujkiewicz, F.W. Sheard and M. Leadbeater, Phys. Rev. Lett. **90**, 110404 (2003).
- [22] R.G. Scott, A.M. Martin, S. Bujkiewicz, T.M. Fromhold, N. Malossi, O. Morsch, M. Cristiani and E. Arimondo, Phys. Rev. A. **69**, 033605 (2004).
- [23] L. Fallani, L. De Sarlo, J.E. Lye, M. Modugno, R. Saers, C. Fort and M. Inguscio, Phys. Rev. Lett. **93**, 140406 (2004).
- [24] Z. Dutton, M. Budde, C. Slowe and L.V. Hau, Science **293**, 663 (2001).
- [25] Clearly, for a symmetrical condensate, $\int dv_x F(v_x - \bar{v}_x) > 0$.